Physics in Medicine &
Biology

Experimental characterization of a diamond detection system for combined dose, LET and RBE assessment in clinical proton beams

To cite this article: C Verona *et al* 2025 *Phys. Med. Biol.* **70** 205012

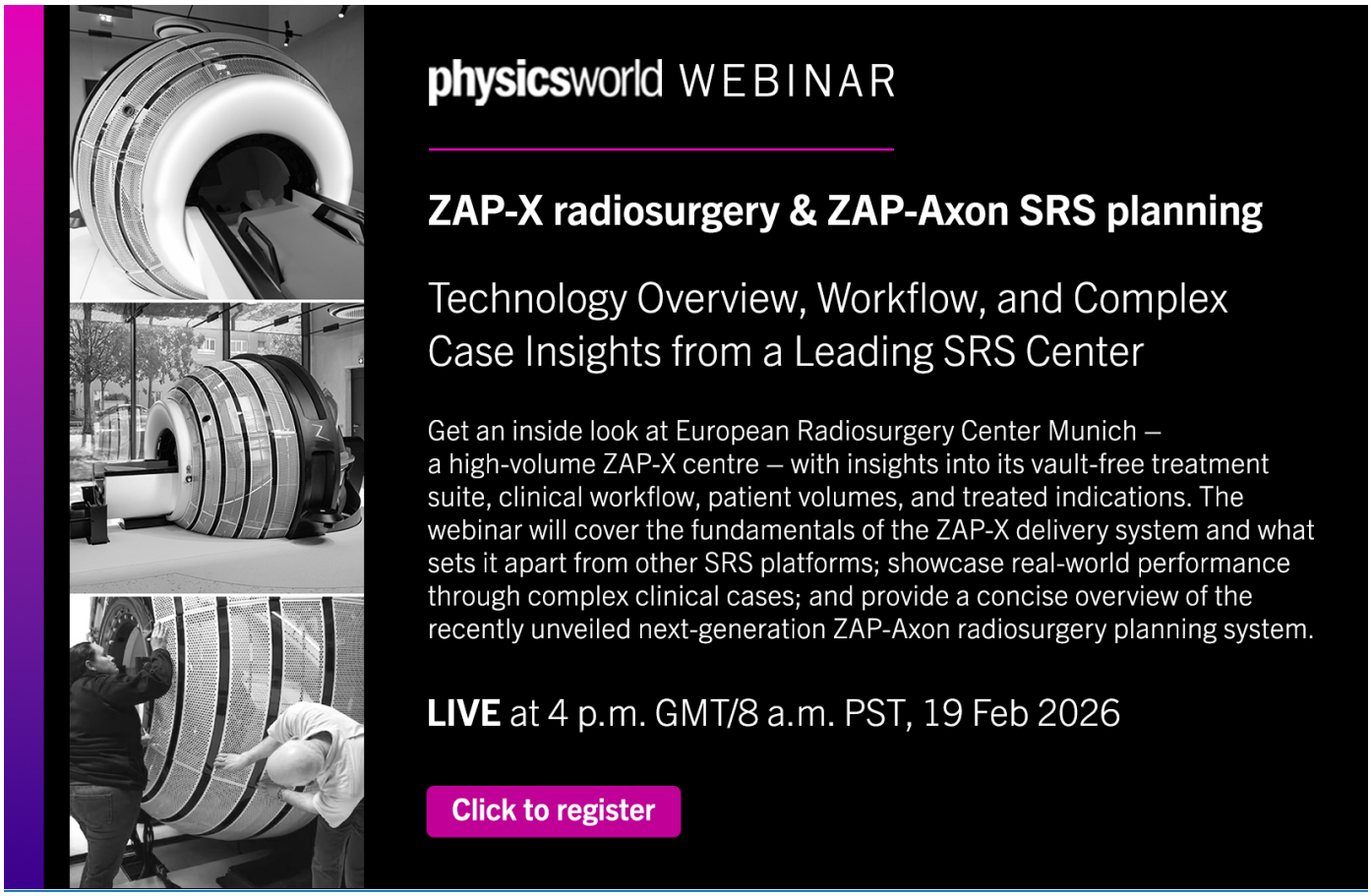

IOP Publishing Phys. Med. Biol. 70 (2025) 205012 https://doi.org/10.1088/1361-6560/ae0be8

Physics in Medicine & Biology

IPEM Institute of Physics and Engineering in Medicine

OPEN ACCESS

RECEIVED
24 April 2025

REVISED
29 August 2025

ACCEPTED FOR PUBLICATION
25 September 2025

PUBLISHED
9 October 2025

PAPER

Experimental characterization of a diamond detection system for combined dose, LET and RBE assessment in clinical proton beams

C Verona[1,*], A Fabbri[2], A Fazzi[3], L Bianchi[3], A Bianchi[4], G A P Cirrone[5], V Conte[4], G Petringa[5], A Raso[1], E Scifoni[6], A Selva[4], F Tommasino[6,7], G Verona Rinati[1] and Enrico Verroi[6]

[1] Dipartimento di Ingegneria Industriale, Università di Roma 'Tor Vergata', Sez. INFN-Roma2, 00133 Rome, Italy
[2] INFN Roma Tre, Via della vasca navale 84, 00146 Rome, Italy
[3] Politecnico di Milano, Dipartimento di Energia, via Lambruschini 4, INFN-Sezione di Milano, Milano, Italy
[4] INFN Laboratori Nazionali di Legnaro, viale dell'Università 2, 35020 Legnaro, Italy
[5] INFN Laboratori Nazionali del Sud, via S. Sofia 62, 95123 Catania, Italy
[6] INFN, Trento Institute for Fundamental Physics and Applications (TIFPA), Povo, TN, Italy
[7] Physica Department, University of Trento, Povo, TN, Italy
[*] Author to whom any correspondence should be addressed.

E-mail: claudio.verona@uniroma2.it

Keywords: diamond, dosimetry, microdosimetry, clinical proton beam, radiation quality

Abstract

Objective. This work presents the first experimental characterization of the DIODE detector, a novel detection system based on single-crystal diamond, designed for simultaneous dosimetric and microdosimetric measurements in clinical proton therapy. The aim is to evaluate its capability to measure absorbed dose, and estimate LET and RBE variations along a clinical proton beam. *Approach.* The detector was tested under a 70 MeV monoenergetic proton beam at the Trento Proton Therapy Centre. Depth-dose and lateral profiles were compared with EBT3 radiochromic films. Microdosimetric spectra were simultaneously acquired and benchmarked against a mini tissue-equivalent proportional counter (TEPC). Monte Carlo (MC) simulations were also performed to model the experimental setup and the DIODE geometry. *Main results.* The detector showed linearity with dose with a sensitivity of 0.60 ± 0.01 nC Gy^{-1}, with a dark current below 0.1 pA, ensuring a good signal-to-noise ratio. Depth-dose profiles matched EBT3 film data and MC simulations, with differences below 2% in peak-to-plateau ratios, indicating limited LET dependence. The dose-mean lineal energy $\bar{y}_D$ closely agrees with simulated dose-averaged LET values, except in the beam entrance region. In this area, $\bar{y}_D$ values were lower than those obtained with the mini-TEPC due to electronic saturation limiting the detection of rare high-LET secondary fragments. Variation in RBE was assessed from the microdosimetric data, based on Loncol's weighting function, which refers to clonogenic cell survival. RBE values ranged from $\sim$1.1 at the entrance to $\sim$1.8 in the distal region, consistent with mini-TEPC data and literature RBE_{10} values for V79 and U89 cells. Lateral dose and microdosimetric profiles confirmed high spatial resolution and revealed proton energy variations near the Bragg peak. *Significance.* The DIODE detector demonstrated reliable performance for simultaneous dosimetric and microdosimetric characterization of clinical proton beams. Its ability to measure dose, and to support LET and RBE assessment through microdosimetric modelling, in a single device, highlights its potential as an advanced tool for beam quality assessment and biologically optimized treatment planning in proton therapy.

1. Introduction

Clinical outcomes collected over the past four decades have suggested that ion therapy has the potential to be a superior treatment modality for several types of cancer. Proton therapy has gained attention for its ability to deliver highly localized radiation with minimal damage to surrounding healthy tissues, thanks to the Bragg peak phenomenon. This effect allows protons to deposit most of their energy at a precise depth, after which the radiation dose rapidly drops to zero, making it particularly effective for tumors near critical structures (Doyen *et al* 2016, Jones *et al* 2018, Ishikawa *et al* 2021, Durante *et al* 2023). Thanks to advances in dose distribution and delivery techniques, proton therapy is gaining increasing global interest as an elective treatment for specific types of tumors, leading to a rapid growth in dedicated facilities. Currently, there are over 120 proton therapy centers worldwide (PTCOG website n.d., as of May 2025). This evolution has highlighted the need for proton dosimetry standardization and improved accuracy, driving the implementation of international dosimetry protocols and the optimization of detector technology.

A key challenge in proton therapy is managing secondary radiation from nuclear interactions between protons and tissue. This fragmentation process produces secondary particles such as neutrons, protons, alpha particles, and heavier ions, which interact differently with tissue, have varying biological effectiveness, and reach their Bragg peak at different depths. As a result, secondary radiation can expose healthy tissues to unintended doses, potentially reducing treatment precision and increasing the risk of long-term side effects, including secondary cancers (Paganetti *et al* 2002, Takata *et al* 2020). The variability in biological effects resulting from the same absorbed dose delivered by different radiation qualities is attributed to the distinctive energy deposition pattern at micrometer and sub-micrometer levels. Therefore, standard dosimetry has significant limitations in proton therapy, as absorbed dose alone is insufficient to fully describe the radiation's biological effectiveness. The treatment planning systems (TPS) are based on the product of the absorbed dose and proper weighting factors accounting for the relative biological effectiveness (RBE) of the radiation (ICRU 2007), established from radiobiological data. In proton therapy, most TPS utilize a fixed RBE value of 1.1, as recommended by the ICRU Report 78 (ICRU 2007). Data presented in literature (Chaudhary *et al* 2014, Paganetti *et al* 2014, 2025, Paganetti *et al* 2019, Tilly *et al* 2021) have shown that proton RBE increases as a function of the water depths, demonstrating that an RBE of 1.1 underestimates the effect of increased LET in the distal region of clinical proton beam.

To optimize treatment outcomes, it is essential to account for LET and RBE variations with depth, in addition to measuring the dose. In this respect, microdosimeters provide valuable tools for calculating and experimentally measuring the physical characteristics of radiation interactions (Kellerer and Chmelevsky 1975, ICRU 1983, Chaudhary *et al* 2014, Tilly *et al* 2021, Braby *et al* 2023), offering a correlation with RBE in a more cost-effective and practical manner compared to traditional radiobiological measurements. Indeed, microdosimetry provides a detailed characterization of energy deposition at microscopic scales, serving as a crucial complement to conventional macroscopic dosimetry (Magrin *et al* 2023).

Both gas detectors and solid-state detectors were used as microdosimeters for clinical ion beam (Verona *et al* 2018, Colautti *et al* 2020, Conte *et al* 2020, Bachiller-Perea *et al* 2022, Tran *et al* 2022, Bortot *et al* 2024, Bianchi *et al* 2025). Although gas-based detectors such as the tissue equivalent proportional counter (TEPC) are considered reference instruments for microdosimetric measurements, they cannot sustain therapeutic fluence rates of 10^9 particles/ cm^2 s, typical of proton therapy. Solid-state detectors, on the other hand, offer advantages such as small physical size, enabling operation in high-intensity beams and providing high spatial resolution. Nevertheless, solid-state detectors also present limitations such as energy/LET dependence, radiation induced damage, and electronic noise, which may degrade resolution and sensitivity, particularly by raising the minimum detectable energy compared to TEPC.

Synthetic single crystal diamond is a good candidate to produce detectors for both dosimetry (Mandapaka *et al* 2013, Marinelli *et al* 2015, Marsolat *et al* 2016) and microdosimetry (Davis *et al* 2014a, Zahradnik *et al* 2018, 2020, Magrin *et al* 2020, Verona *et al* 2020, Parisi *et al* 2024) of ion beams thanks to its outstanding properties such as low dielectric constant, near-tissue equivalence, near-constant stopping power ratio with respect to water (Davis *et al* 2019, Songke *et al* 2022) and high radiation hardness (Verona *et al* 2015). On the other hand, diamond's higher mean ionization energy (∼13 eV *vs.* 3.6 eV for silicon) results in lower signal amplitudes, reducing the signal-to-noise ratio.

Recently, a novel compact detection system embedding a single crystal diamond dosimeter and a microdosimeter in the same device, thus providing simultaneous dosimetric and microdosimetric capabilities, was developed in the framework of INFN project, called DIODE (Verona *et al* 2024).

In this work, the DIODE detector was characterized for the first time under a 70 MeV proton beam at the research beamline in Trento. Dosimetric and microdosimetric data were acquired simultaneously and at the same depth in a water-equivalent phantom. The detector's response was compared with conventional detectors, specifically EBT3 gafchromic films for dosimetric response evaluation, and the miniaturized TEPC

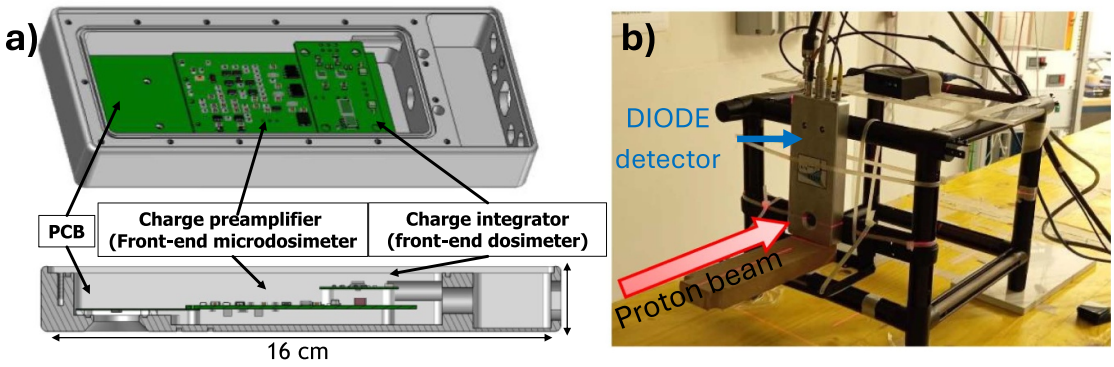

Figure 1. (a) Layout of the developed DIODE detector in the framework of the INFN-CSNV project. (b) Picture of the experimental setup at the Trento Proton Therapy Centre.

(mini-TEPC) from LNL-INFN for microdosimetric response assessment. Additionally, Monte Carlo (MC) simulations using the Geant4 toolkit were developed to replicate the experimental data, modelling the full geometry of the detector and the proton beam used during the measurements.

2. Materials and methods

2.1. DIODE device

The DIODE detector is based on synthetic single-crystal diamond and operates in two distinct modes: current-integration mode for dose measurements and pulse mode for single-event energy deposition measurements. The active elements of the detector are engineered as Schottky diodes integrated on the same diamond substrate ($3 \times 3 \times 0.3$ mm^2 in size), featuring an application-specific, optimized layout to enhance performance. For this experiment, the diamond-integrated detector comprises: (i) a dosimeter (Dos) with a sensitive area of approximately 3.4 mm^2 and a thickness of about 0.70 ± 0.05 μm, designed for dosimetric measurements, and (ii) a microdosimeter (μDos) with a sensitive area of 0.038 mm^2 and a thickness of 6.3 ± 0.2 μm, tailored for microdosimetric measurements. The detector thicknesses were estimated by capacitance-voltage measurements and analysing the detector response to α-particles from a collimated ^{241}Am source as a function of the incidence angle, as reported in literature (Verona *et al* 2015, Marinelli *et al* 2016). The diamond-integrated detector was micro-bonded in a PCB made in Teflon and placed inside an aluminium box (hermetically sealed) coupled with the two readout chains. A schematic view of the DIODE detector is reported in figure 1(a). The detector was encapsulated in epoxy resin (corresponding to 2.7 mm of water equivalent (WE) thickness) to prevent air ionization from affecting the dosimetric response and to ensure waterproofing. Dedicated front-end electronic circuits both for dosimetric and microdosimetric signals are housed within the Al enclosure to minimize noise and enhance device compactness. More detail of DIODE detection system is described in Verona *et al* (2024).

Measurements were performed with the μDos biased at +20 V and the Dos operating in unbiased mode. For the dosimetric signal, an external microcontroller controls the integration time, while a 16-bit A/D converter samples the integrator output at the beginning and end of each integration period, defined by two reset pulses. The integration time was fixed to 500 ms. The μDos signal is integrated by means of a custom-made charge-sensitive preamplifier with a high sensitivity of about 7.7 V/pC. The voltage output was then fed to a shaping amplifier (Silena 7611) set with 200 gain and 2 μs shaping time. The pulse height spectra for incident protons were measured using an ORTEC Easy-MCA multichannel analyser connected to a portable computer. Energy calibration was previously performed using a calibrated pulse generator to convert the channel number to the imparted energy. The calibration with a pulse generator was conducted by using a 25 μm thick single crystal diamond detector, having the same geometry and similar capacitance of the μDos, exposed by alpha particles emitted from an ^{241}Am source (mean energy of 5.5 MeV with an approximate range of 13 μm in diamond). The adopted electronic readout chain allowed the μDos to detect signals above the noise level as low as approximately 7.5 keV and to measure maximum energies up to 1.25 MeV in diamond.

2.2. Experimental set up

The DIODE detector was tested at the Trento Proton Therapy Centre (Italy), which is operated in collaboration with TIFPA (Trento Institute for Fundamental Physics and Applications, INFN), using a

quasi-monochromatic 70 MeV proton beam on the 30° beamline, commonly referred to as the Physics beamline (Tommasino *et al* 2017). This line is designed for physics experiments and provides a narrow pencil beam. The proton beam at 70 MeV exhibits a Gaussian spatial profile with $\sigma \approx 6.93$ mm at isocenter. Given the small sensitive diameters of the Dos (∼2.3 mm) and μDos (∼220 μm) detectors, the proton fluence can reasonably be considered quite uniform over the detector active areas.

The detector was aligned using a laser-based reference system at the isocenter, located 1.25 m from the beam exit window. The experimental setup is pictured in figure 1(b). The nominal beam current was 10 nA and it was increased to 50 nA for measurements carried out in the distal fall-off region of the Bragg peak, in order to improve the statistics.

Energy spectra and current were simultaneously acquired using the DIODE detector at each position. The current and the total charge generated in the sensitive volume (SV) of the Dos were recorded by custom-built software upon completion of the proton irradiation. Meanwhile, the energy-deposition distribution in the SV of the μDos was collected on an event-by-event basis, with approximately 3×10^6 events registered during the whole irradiation period.

Twenty-three distinct WE depths were obtained by interposing a variable number of calibrated EBT3 gafchromic films (3×3 cm^2 in size, each with a known thickness of 0.355 mm WE) in front of the DIODE detector. This configuration allowed precise sampling along the Bragg peak region. The films were held firmly using a PMMA support, allowing stable and reproducible positioning. The density of the measuring positions increases at the distal and fall-off regions of the Bragg peak where the radiation quality varies more rapidly. The total WE depth was calculated accounting for the WE thickness of the EBT3 layers and the epoxy resin layer in front of the detector, i.e. ∼2.7 mm. The twenty-three WE depths resulted to be 3.05, 8.38,11.22,18.68, 23.64, 28.97, 34.29, 35.00, 35.71,36.42, 36.78, 37.13, 37.49, 37.84, 38.20, 38.55, 39.26, 39.62, 39.97, 40.33, 40.68, 41.04 and 41.39 mm. The resulting positioning error was ±0.20 mm and includes the uncertainty stemming from the positioning and the calculation of the WE thickness of the materials in front of the detector.

The EBT3 films were also used as an independent relative dosimetric system to benchmark the DIODE detector response. Indeed, a separate setup composed of a stack of 120 EBT3 films was employed to measure the depth dose curve, the lateral dose profile of the proton beam as well as to reconstruct the incident proton energy spectrum. The films were calibrated in terms of dose in water, with doses ranging from 1 Gy to 20 Gy, using monochromatic proton beams at energies of 30 MeV and 70 MeV. All films were analysed 24 h after exposure, following the procedure described in Cirrone *et al* (2020). They were scanned using an EPSON Expression Photo Scanner, Model 10000XL. The red colour channel and a resolution of 169 μm were selected as the main imaging parameters, in accordance with the recommendations in the EBT3 datasheet. In addition, Giraffe detector (IBA Dosimetry), a multilayer ionization chamber array composed of 180 sensitive layers (WE thickness of approximately 1.9 mm per channel), was employed to measure the depth-dose profile along the central axis of the beam.

A mini-TEPC developed by LNL-INFN, was used for intercomparison of measured distributions. It is a miniaturized cylindrical TEPC of 1 mm in diameter and height, filled with propane gas at a pressure of 408 hPa to simulate 1 μm thick of biological tissue. A detailed description of the detector characteristics and performances can be found in previous works (Bianchi *et al* 2021b, Bianchi *et al* 2024).

2.3. Data analysis

The energy spectra acquired from the microdosimeters were analysed to extract relevant microdosimetric quantities. A key parameter in microdosimetry is the lineal energy, y, as defined in ICRU Report 98 (Braby *et al* 2023). Lineal energy is computed as $\frac{\varepsilon_{\mathrm{dep}}}{\bar{l}}$, where $\varepsilon_{\mathrm{dep}}$ is the energy deposited in the SV of the detector during a single event, and $\bar{l}$ represents the mean chord length within that SV. For μDos, due to their slab-like geometry and the unidirectional nature of the proton beam, the mean chord length, corresponding to the detector SV thickness, was considered in the definition of lineal energy, as previously discussed by Solevi *et al* (2015). The microdosimetric spectra were represented as $y\mathrm{d}(y)$ vs. y, where $\mathrm{d}(y)$ is the lineal energy dose distribution. The dose distribution is mathematically defined as $d(y) = \frac{y}{\bar{y}_{\mathrm{F}}} f(y)$, where $f(y)$ is the lineal energy probability density function, and $\bar{y}_{\mathrm{F}}$ is its expectation value, known as the frequency-mean lineal energy. Following the methods presented in Lindborg and Waker (2017), this quantity is expressed as $\bar{y}_{\mathrm{F}} = \int_{y_{\min}}^{\infty} y f(y)\,\mathrm{d}y$. The second moment of the frequency distribution, which corresponds to the expectation value of $\mathrm{d}(y)$, is referred to the dose-mean lineal energy and is calculated as $\bar{y}_{\mathrm{D}} = \int_{y_{\min}}^{\infty} y\mathrm{d}(y)\,\mathrm{d}y = \int_{y_{\min}}^{\infty} \frac{y^2}{\bar{y}_{\mathrm{F}}} f(y)\,\mathrm{d}y$. We have indicated the low lineal energy threshold or cut-off in lineal energy as $y_{\min}$, which accounts for background noise in the experiment.

Finally, the ability of the DIODE detector to assess RBE variations was also analysed using microdosimetric data. The *in vitro* clonogenic cell survival RBE_{10} (RBE relative to a surviving fraction of

10%) for V79 cell line was estimated based on the experimentally measured $d(y)$, applying Loncol's biological weighting function $r(y)$ (Loncol *et al* 1994). According to the model formalism, this estimation follows $RBE = \int_{y_{min}}^{\infty} r(y)\, d(y)\, dy$. Although $r(y)$ was originally derived for a specific biological endpoint (early intestinal intolerance assessed by crypt regeneration in mice *in vivo*), it has been shown to accurately reproduce RBE_{10} variations as a function of depth for clonogenic assays of several radio-resistant cell lines as well (De Nardo *et al* 2004). This approach was already employed for other solid state and gas microdosimeters in other experiments (Conte *et al* 2020, Bortot *et al* 2024).

3. MC simulation

MC simulations using Geant4 toolkit (Agostinelli *et al* 2003, Allison *et al* 2006, 2016) were performed to support the experiment and for modelling the detector. MC simulations were conducted to determine the expected proton energy spectrum in the SV of the μDos, the water-equivalent thickness of the μDos and to verify that the mean values obtained from the microdosimetric spectra were consistent with the expected LET values.

3.1. Diamond-to-water conversion

To convert the energy spectrum in diamond into the microdosimetric spectrum in water, it is necessary to evaluate the water-equivalent mean chord length of the μDos. This was determined using a custom Geant4 application following the methodology proposed by Davis *et al* (2014b, 2019).

A detailed simulation of the μDos layout was first developed, including the inactive diamond substrate (300 μm in thickness), the Schottky Cr contact layer (50 nm thick) and the active diamond detection region (6, 3 μm thick and 110 μm in radius). The Geant4 model accounted for both electromagnetic and elastic and inelastic hadronic interactions of incident protons, as well as secondary particles produced within the water phantom. Hadronic interactions were simulated using the G4HadronElasticPhysicsHP, G4IonElasticPhysics, G4HadronPhysicsQGSP_BIC_HP, and G4IonPhysicsPHP models, while electromagnetic interactions were described by the G4EmStandardPhysics_option4 package.

The mean chord length in water was derived through an iterative two-step simulation procedure. In the first step, the proton energy deposition was simulated in the active diamond layer. In the second step, a simulation under identical irradiation conditions was performed by replacing the diamond layer with water. The equivalent water thickness was iteratively adjusted until the simulated proton spectra in diamond and water agreed. An example is shown in figure 2(a). The resulting WE thickness corresponding to this agreement was adopted as the mean chord length in water. The mean chord length in water as a function of the depth in water is shown in figure 2(b) for 70 MeV protons. The error bars represent the variation in mean chord length corresponding to a 1% difference between the centroids of energy spectra in diamond and water.

The mean chord length values remain nearly constant at approximately 20.15 μm, with a variation of less than 0.5% across the entire water depth range. The slight increase of the mean chord length in water at greater depths, corresponding to lower proton energies, is mainly due to a small increase in the diamond-to-water stopping power ratio.

3.2. Absorbed dose and LET

Expected Dose and LET variations for the adopted irradiation setup were calculated using the *Hadrontherapy* toolkit (Cirrone *et al* 2011). This open-source application, developed for dosimetric and radiobiological studies with proton and ion beams, implements validated algorithms to calculate key radiobiological quantities. In particular, the averaged total LET-track and total LET-dose, which considering secondary particles produced in the interaction of the primary proton with the water, was simulated following the procedure reported in Petringa *et al* (2020). The source term was customized to replicate the experimental conditions, modelling the proton beam as a circular spot with a bivariate Gaussian spatial distribution ($\sigma = 2$ mm) and an angular spread ($\sigma = 0.028°$). The proton beam energy was centred at 68.8 MeV with an energy spread of 0.6 MeV. Simulations were carried out using Geant4 version 10.08.p02 (May 2024), with each run consisting of 10^7 primary events. To reconstruct the LET distributions, a voxelized water phantom was implemented at the beam exit, reproducing a typical water tank geometry used in clinical dosimetry. The phantom was segmented into $400 \times 400 \times 0.01$ mm^3 slices orthogonal to the beam axis. A range cut of 0.1 mm was applied for secondary particle production, and the maximum allowed step size was set to 0.1 mm to ensure high spatial accuracy.

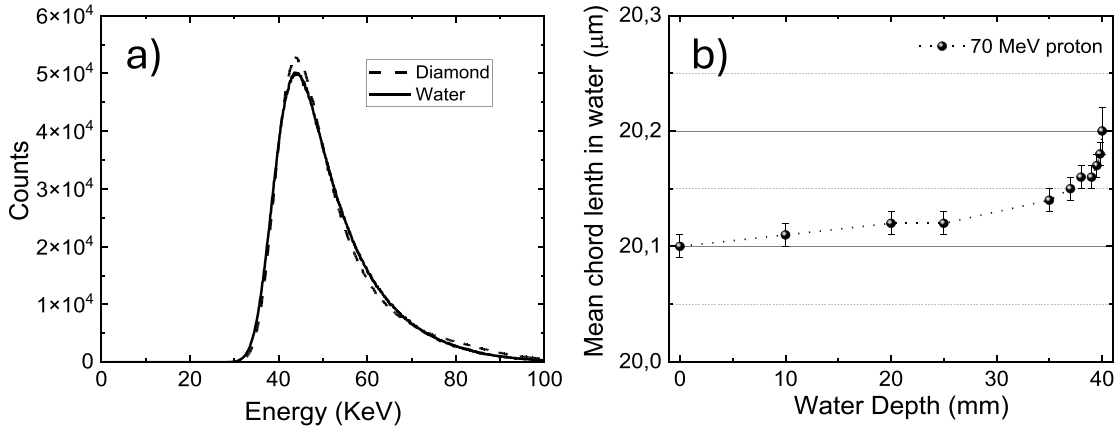

Figure 2. (a) Energy deposition distribution within the SV of the detector: in diamond (dashed line) and in equivalent water (solid line). (b) The mean chord length in water of the DIODE detector as a function of the depth in water for 70 MeV proton beam.

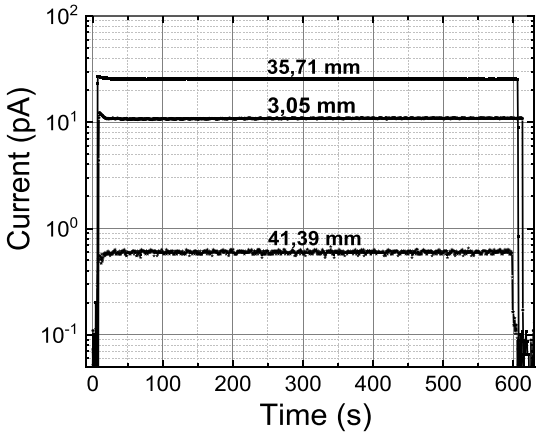

Figure 3. Time response of the DIODE detector at different water equivalent depths.

4. Results and discussion

4.1. Time response and linearity

Figure 3 shows the current curves recorded by the DIODE detector during 600 s irradiations at three different WE depths. The plateaus of these curves reflect the relative dose rate of the proton beam employed. The measured current varied with water depth, ranging from fractions of pA to several tens of pA, and exhibited a high signal-to-dark ratio. Under beam-off conditions, the DIODE detector showed a very low dark current, remaining below 0.1 pA, compatible with the leakage current of the electronic system readout. The induced charge, corresponding to the relative absorbed dose, was determined by integrating the current signal over the irradiation period. To verify the reproducibility of the dose measurements, three irradiations were conducted under identical conditions, with the variation among measured values consistently remaining below 2% for each profile point.

The linearity of the DIODE detector response was tested in the entrance region, i.e. at ∼3 mm WE depth. In figure 4(a), the charge measured by the DIODE detector is plotted against the delivered dose up to about 11 Gy, along with the corresponding linear fit. The delivered dose was measured using EBT3 films irradiated in the same condition. An error bar of ±5% was adopted for the EBT3 dose determination. Such a value was estimated by repeatability tests and the intrinsic uncertainty of the EBT3 readings.

The coefficient of determination for the linear regression (R^2) was 099 984, demonstrating a good linearity of the detector in the whole investigated dose range. Deviation from linearity of the detector response, calculated as percentage deviation of charge readings with respect to those resulting by the linear best fit, was within 2% in the whole investigated dose range (see bottom of figure 4(a)). The sensitivity of the detector, derived from the slope of the linear fit, was found to be about 0.60 ± 0.01 nC Gy^{-1}. To verify the consistency of this result with the expected value, we used the following equation $S = \frac{\rho_{dia} A_{Dos} de}{w}$, were ρ_{dia} is

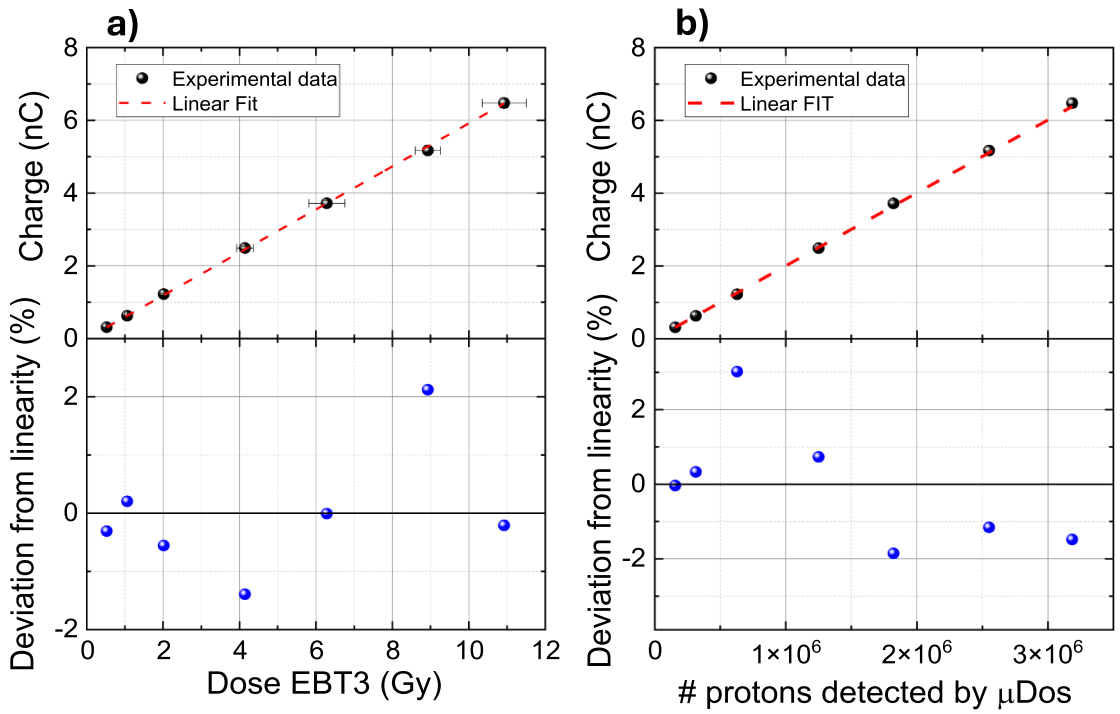

Figure 4. (a) Upper plot: charge measured by the DIODE detector as a function of proton delivered dose, estimated by EBT3 film, at the entrance of the full-energy proton beam. Lower plot: percentage deviation from linearity. (b) Upper plot: the charge measured by the DIODE detector as a function of the number protons impinging on the μDos at the entrance region. Lower plot: percentage deviation from linearity.

the density of diamond (3510 kg m^{-3}), A_{Dos} is the sensitive area of the Dos ($3.4 \cdot 10^{-6}$ m^2), d is the thickness of the Dos (0.70 ± 0.05 μm), e is the elementary charge and w is the mean energy required to create an electron–hole pair in diamond ($2.1 \cdot 10^{-18}$ J i.e. 13.2 eV (Schmid *et al* 2004)). The expected sensitivity is approximately (0.64 ± 0.05) nC Gy^{-1}, is compatible with the measured value, within the uncertainty mainly originated from the sensitive thickness of the Dos.

The charge is plotted in figure 4(b) as a function of the total number of protons impinging on the μDos, obtained from the number of events acquired by the μDos at the different delivered doses. The data shows a linear trend of charge as a function of the number of incident protons, with a deviation from linearity within 3%, as estimated in the bottom panel of figure 4(b). From the slope of the linear fit, the charge Q_{p} released by a single proton in the Dos can be calculated. Indeed, considering the area ratio between the Dos and the μDos $\left(\frac{A_{\mathrm{Dos}}}{A_{\mu\mathrm{Dos}}} = 89\right)$, we obtain a charge value of approximately $(2.30 \pm 0.07) \cdot 10^{-17} C$. Using the equation $Q_{\mathrm{p}} = \frac{S_{\mathrm{dia}} ed}{w}$, where S_{dia} the proton stopping power in diamond ($\sim$3 keV μm^{-1} for 70 MeV protons), it is possible to determine an expected charge of $(2.55 \pm 0.18) \cdot 10^{-17}$ C, which is in agreement with the experimental one.

These findings highlight the consistency and reliability of the DIODE detector under proton irradiation conditions supporting the validity of the measurement method.

4.2. Depth dose profiles

Figure 5 shows the relative depth-dose curve measured with the DIODE detector (blue dots) for a quasi-monoenergetic 70 MeV proton beam. Additionally, the depth-dose distribution was obtained using a stack of 120 calibrated EBT3 radiochromic films (red dots), irradiated for 30 s to avoid signal saturation, and with the Giraffe detector (opened stars). The MC simulated dose profile (represented by the continuous line) closely reproduces the measured dose profile for a proton beam energy of 68.8 MeV with an energy spread of approximately 600 keV. All curves are normalized to the signal at a depth of 3 mm in the entrance region of the Bragg curve. In this study, EBT3 films were reconstructed using a single entrance-region calibration with no explicit LET-dependent correction. As observed, a reasonable agreement between the depth–dose curves obtained with all detectors and MC simulation is observed, except in the Bragg-peak region, where the well-documented LET-dependent quenching of Gafchromic films leads to an 20% underestimation of dose for EBT3 and a lower peak-to-plateau ratio, consistent with reports for EBT2 and EBT-XD (Perles *et al* 2013, Guan *et al* 2023). This effect, attributed to the saturation of ionization events in the film's sensitive layer,

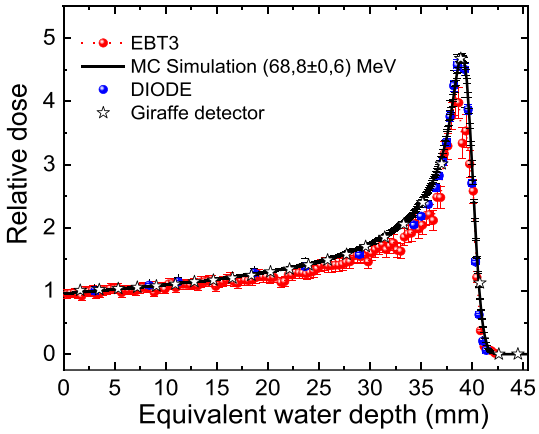

Figure 5. Central-axis relative depth dose curves measured by the DIODE and the EBT3 film for 70 MeV proton beam. The depth dose curve simulated by Monte Carlo is also reported.

Table 1. Analysis parameters for depth dose curves reported in figure 6.

	R90 (mm)	DDF (80%–20%) (mm)	Peak-to-plateau ratio
DIODE	39.5 ± 0.2	0.9 ± 0.2	4.60 ± 0.18
EBT3	39.20 ± 0.35	1.30 ± 0.35	3.98 ± 0.27
MC	39.5	1	4.69

reduces its response to the actual deposited dose, with the largest variation occurring at the distal end of the depth-dose curve across the Bragg peak (Padilla-Cabal *et al* 2019). In addition, a small under-deviation is observed in the proximal region of the Bragg peak for both the DIODE and the EBT3 detectors. This discrepancy can be attributed to multiple factors, including the uncertainty in detector positioning and the estimation of the water-equivalent thickness of the materials in front of the detectors.

A quantitative analysis of the measured depth dose curves is provided in table 1, based on the parameters recommended by ICRU Report No. 78 (ICRU 2007): (i) penetration depth R90 (position in the distal fall-off of the Bragg curve where the dose is reduced to 90% of the peak maximum) (ii) distal-dose falloff distances DDF(80%–20%), and (iii) peak-to-plateau ratios for the proton beam.

The values calculated by the DIODE detector are in agreement with the MC ones, within the experimental position errors, and with those reported by Tommasino *et al* (2017), for the physics beamline at the Trento Proton Therapy Facility. The peak-to-plateau ratio values measured by the DIODE detector and the MC simulation were found to agree within 2%, compatible with experimental uncertainties. It should be notice, however, that the Bragg peak may not be fully resolved due to the 0.355 mm depth interval, potentially affecting the precision of the measured peak-to-plateau ratio.

It is important to note that a depth-dose curve serves as a comprehensive test of the detector's dose linearity, energy and LET dependence. As demonstrated earlier, the DIODE response is linear with the absorbed dose. These results suggest that the DIODE detector exhibits a stable response across the investigated energy and LET range, with no significant deviations observed from about 70 MeV down in entrance to the Bragg peak region The DIODE's favourable LET independence can be attributed to the Dos extremely thin, high-quality SV as also discussed in Mandapaka *et al* (2013).

4.3. Microdosimetric spectra

Figure 6 illustrates the microdosimetric spectra acquired by the DIODE detector for the different measurement positions along the proton Bragg peak. The absorbed dose distributions are displayed as $yd(y)$ versus y on a logarithmic scale to enhance visualization and interpretation. In this representation, the area under the curve between two lienal energy values quantifies the fraction of the absorbed dose associated with the energy deposition events within that interval (Conte *et al* 2020). The dark blue curves, positioned on the left, represent measurements taken in the entrance region, the light blue and green spectra are in the proximal region, while the red curves on the right correspond to measurements beyond the Bragg peak. In particular, the proton beam generated lineal energies ranging from 0.3 to 7 keV μm^{-1} at the entrance, 1 to 10 keV μm^{-1} in the proximal region of the Bragg peak, and 0.5 to 45 keV μm^{-1} in the distal region of the Bragg peak.

At the entrance of the Bragg peak, where proton energy is still high and LET remains low, the signal-to-noise ratio was sufficient to obtain reliable microdosimetric spectra. Indeed, the spectra show a low

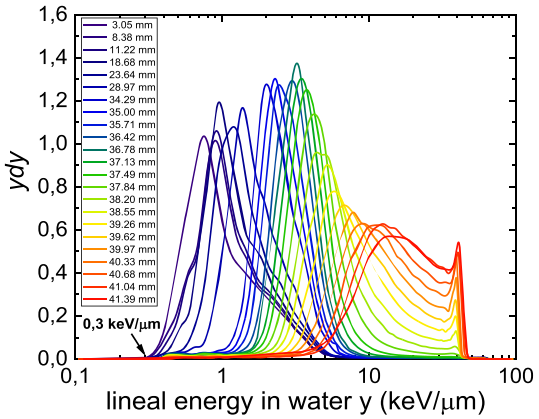

Figure 6. Microdosimetric spectra, $yd(y)$ vs y, acquired by DIODE at different water equivalent depths.

cut-off around 0.3 keV μm^{-1}, corresponding to the electronic noise threshold of the detection system during irradiation. This value is significantly lower than those reported in the literature for diamond microdosimeters, which typically exhibit cut-off values closer to 1 keV μm^{-1} or higher (Magrin *et al* 2020, Verona *et al* 2020, Parisi *et al* 2024). For DIODE detector, electromagnetic and electronic noise is minimized by placing the front-end electronic readout system inside an encapsulated housing that encloses the detector.

As observed, the microdosimetric distributions shift towards higher lineal energy values with increasing depth in water. This occurs due to the well-known increase in proton LET near the distal edge. This trend reaches its peak near the Bragg region, where ionization density is at its maximum as the protons come to rest, marking the region of highest energy deposition before the dose rapidly falls off. This feature appears at the far right of the spectra, the so-called proton edge, where the distributions abruptly drop to zero. The proton edge represents the maximum lineal energy that a proton can deposit within the SV of the detector. In the μDos with an active thickness of 6.3 μm, protons deposit a maximum energy of approximately 860 keV. This corresponds to a lineal energy in water of about 43 keV μm^{-1}.

A comparison was carried out between experimental data and MC simulations performed using Geant4. Figure 7 presents the microdosimetric spectra measured with the DIODE detector and the corresponding Geant4 simulations at four WE depths, i.e. 11.22 mm and 28.97 mm (entrance region), 38.20 mm (Bragg Peak region), and 40.68 mm (falloff region). The simulations were adjusted to take into account the border effects of the SV of the μDos, as reported in Parisi *et al* (2025). A border effect of 3.5 μm was considered in the simulation. The experimental border effect was measured using the ion beam induced charge technique on a similar 6 μm thick diamond microdosimeter, irradiated with 1.8 MeV protons (Parisi *et al* 2025).

Overall, the experimental and simulated data show a strong agreement in both the shape of the spectra and the positioning of lineal energy values, with only a minor discrepancy observed at low lineal energy values, just before the low-energy cut-off, where the noise is more relevant. As clearly seen in figure 7, at the entrance regions, the MC simulated spectra exhibit rare high lineal energy events (in the range 100–1000 keV μm^{-1}). Such events are attributed to nuclear interactions, secondary particle production, and proton-induced fragmentation. Indeed, elastic and inelastic nuclear collisions generate high-LET secondary particles, which are expected to deposit significantly higher lineal energy than the primary protons. These high-energy events were not detected experimentally by the DIODE detector due to saturation of the electronic chain used during the measurements, which prevented the recording of events exceeding 65 keV μm^{-1}. However, as demonstrated by MC simulations, the detector is potentially capable of measuring such events, provided that the electronic system is optimized to extend the detectable energy range (e.g. by reducing the gain)

Given the critical role of secondary fragments in shaping biological effects, it is essential to implement a dual electronic acquisition system with different gain settings or an extended dynamic-range of the electronics system. This approach ensures the accurate detection of both primary protons and rare high-energy secondary fragments, enabling precise microdosimetric characterization, which is fundamental for assessing their radiobiological impact.

Figure 8(a) shows microdosimetric spectra measured with the mini-TEPC and the DIODE detector at two different water depths, i.e. entrance region (∼18 mm) and fall-off region (∼40 mm). The positions of the lineal energy peak resulting from the electromagnetic interactions of primary protons are consistent between the two detectors. Differences in spectral shapes arise mainly due to variations in the geometry and

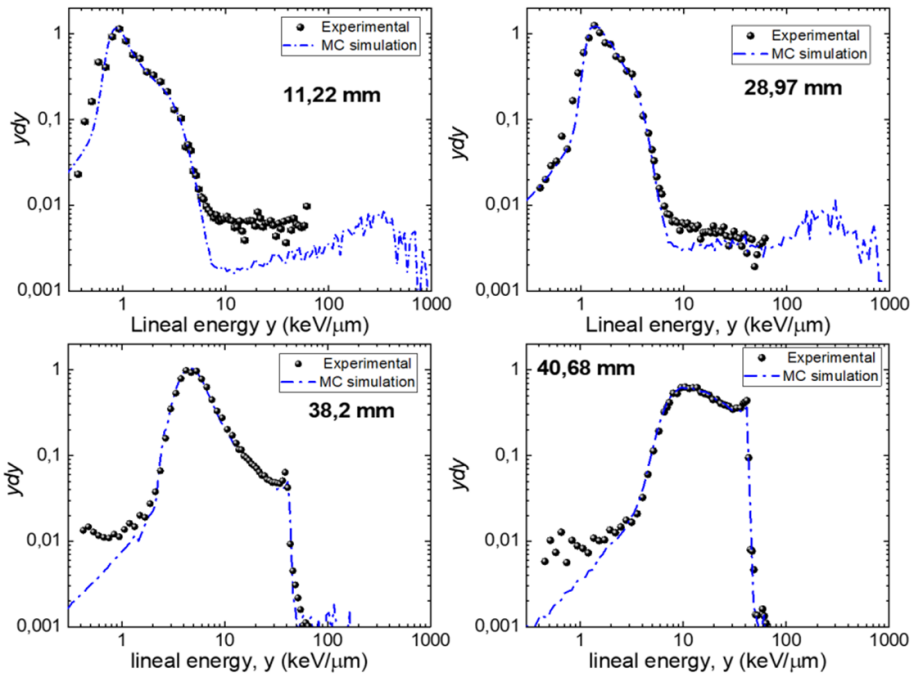

Figure 7. Experimental and simulated $y\mathrm{d}(y)$ vs y at four water equivalent depths.

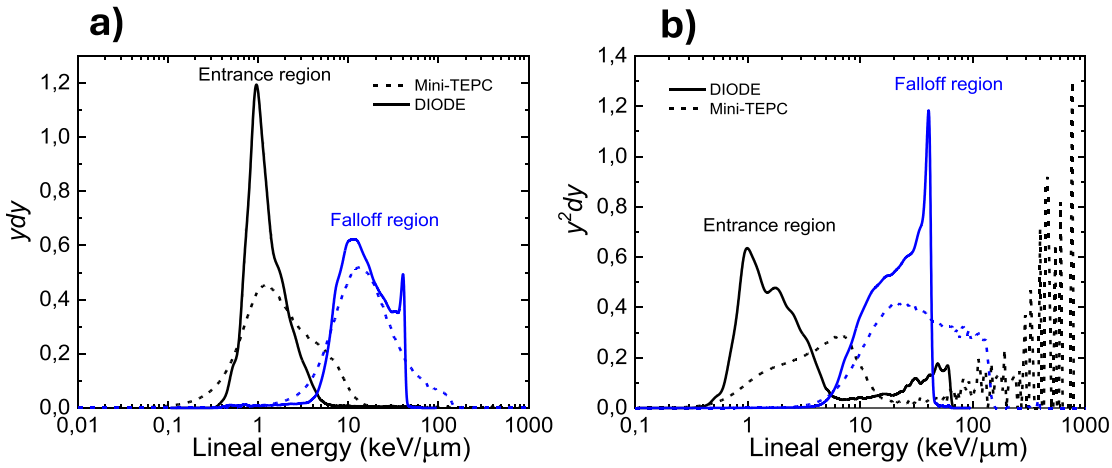

Figure 8. (a) The $y\mathrm{d}y$ and (b) $\frac{y^2\mathrm{d}(y)}{\bar{y}_\mathrm{D}}$ distributions measured with the DIODE and the mini-TEPC at the entrance and falloff regions.

size of their SVs. The μDos, having a slab geometry, exhibits a path-length distribution of primary particles that closely resembles a Dirac delta function at its thickness. In contrast, the mini-TEPC, with its cylindrical geometry, has a much broader distribution, peaking at the diameter size and extending into a long tail toward smaller chord lengths. Furthermore, energy-loss straggling is more pronounced in thinner SVs, contributing to the broader lineal energy spectrum observed in the mini-TEPC. Notably, the events in the 3–10 keV $\mu\mathrm{m}^{-1}$ range in the mini-TEPC spectra are attributed to secondary δ-electrons generated outside the SV. This contribution is not observed in the μDos due to its larger SV, where electron signals are overshadowed by those of primary protons. Similar differences were observed between other solid-state microdosimeters and mini-TEPC at the CATANA beam line (Bianchi *et al* 2023a).

Due to their rarity, high lineal energy events exceeding 20 keV $\mu\mathrm{m}^{-1}$ in lineal energy are not easily distinguishable in the conventional $y\mathrm{d}(y)$ representation. However, they became more apparent in the $y^2y\mathrm{d}\,(y)\,/\bar{y}_\mathrm{D}$ representation, employed also in other beam quality (Conte *et al* 2020, Bianchi *et al* 2023c, Bianchi *et al* 2023b) as shown in figure 8(b). In such representation, equal areas under the curve correspond to equal contributions to the dose mean lineal energy, $\bar{y}_\mathrm{D}$. It is clearly observed in figure 8(b) that, in the case of the mini-TEPC, these rare fragments have a significant impact on $\bar{y}_\mathrm{D}$ at a depth of 18 mm, increasing its

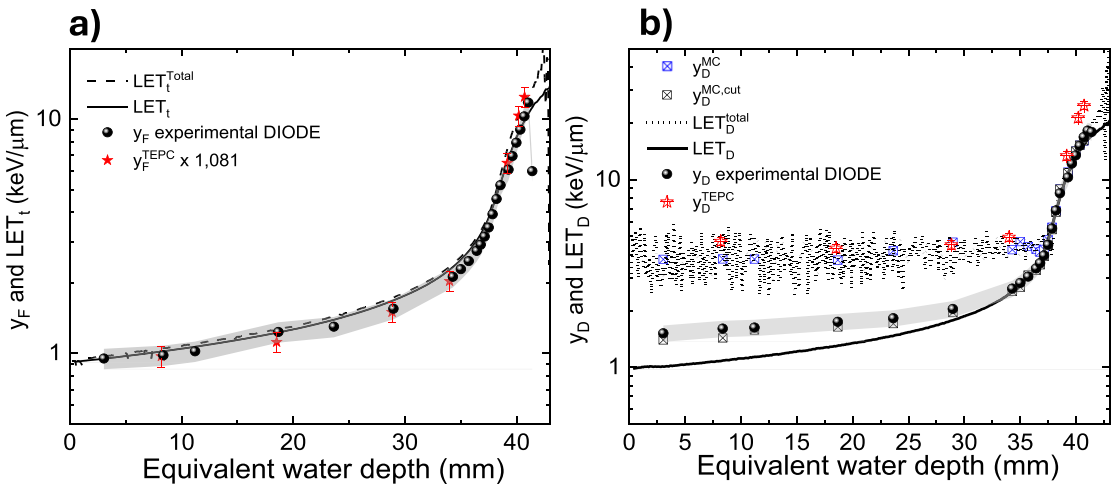

Figure 9. (a) The frequency mean lineal energy, $\bar{y}_F$, derived from the microdosimetric spectra, compared to the results of Geant4 Monte Carlo simulations for the track-averaged LET (continuous line) and the total track-averaged LET (dashed line). Filled circles: DIODE; filled stars: mini-TEPC. (b) Dose mean lineal energy derived from the experimental ($\bar{y}_D$) and simulated microdosimetric spectra ($\bar{y}_D^{MC}$), compared to the results of Monte Carlo simulations for the dose-averaged LET (solid line) and the total dose-averaged LET (dashed line). Solid circles: DIODE; solid stars: mini-TEPC; open blue square: Monte Carlo simulation; open black square: Monte Carlo simulation with the cut at 65 keV μm^{-1}.

overall value. Conversely, in the DIODE detector, the electronic readout chain saturation leads to a lower $\bar{y}_D$. At a depth of 40 mm (fall-off region), the contribution from high-energy deposition events other than those of primary particles becomes negligible, resulting in more consistent $\bar{y}_D$ values between the two detectors.

4.4. Dose and frequency mean energy values and LET

The dose-mean and frequency-mean lineal energy, $\bar{y}_D$ and $\bar{y}_F$ respectively, were derived from the microdosimetric spectra following the methodology detailed in section 2.3. The obtained values were compared with the average LET values calculated through MC simulations, with the aim of assessing the potential applicability of the DIODE detector for quality assurance in LET-based treatment planning systems.

Figure 9(a) presents the experimental $\bar{y}_F$ values in comparison with the average LET track (LET_T), while figure 9(b) illustrates the experimental $\bar{y}_D$ values and the simulated average LET dose (LET_D). A grey error band is shown to represent the uncertainty associated with $\bar{y}_D$ and $\bar{y}_F$, arising from the propagation of errors related to energy calibration of the electronic chain, diamond SV thickness as well as the diamond-to-water conversion. The total uncertainty on the mean lineal energy values was estimated to be approximately 10% (Meouchi *et al* 2022). In addition, the total average LET values (LET_D^{total}, LET_T^{total}) account for the contribution from secondary particles, including ions and other nuclear fragments, are plotted. In both the figures, $\bar{y}_D^{TEPC}$ and $\bar{y}_F^{TEPC}$ obtained using the mini-TEPC, are also reported for comparison. In this work, the values for $\bar{y}_F^{TEPC}$ were corrected only for the geometric chord length factor, which is $32/3\pi^2 \cong 1.081$ as reported in Kellerer and Chmelevsky (1975), for a cylinder of equal diameter and height irradiated by a parallel beam orthogonally to its axis. The uncertainty assigned to $\bar{y}_F^{TEPC}$, which is significantly influenced by the extrapolation of data to 0.01 keV μm^{-1} (Bianchi *et al* 2021a), was 10%, while the uncertainty on $\bar{y}_D^{TEPC}$, evaluated from repeated measurements, was found to be 5%. These uncertainties do not account for potential systematic errors, such as those arising from the linear energy calibration of the spectra.

The $\bar{y}_F$ measured with the DIODE detector is approximately 1 keV μm^{-1} at the entrance region and gradually increases, reaching a peak of about 15 keV μm^{-1} in the distal fall-off region. The $\bar{y}_D$ values show a progressive increase, reaching approximately 10 keV μm^{-1} in the Bragg peak region and peaking at around 20 keV μm^{-1} in the distal fall-off region.

The $\bar{y}_F$ measured by the DIODE detector remains consistent with the values obtained using the mini-TEPC throughout the entire water depth. Moreover, the measured $\bar{y}_F$ values agree, within experimental uncertainty, with both the LET_T and LET_T^{total} values, further validating the accuracy of the microdosimetric measurements. On the other hand, the $\bar{y}_D$ values remain lower than LET_D^{total} and the $\bar{y}_D^{TEPC}$ in the entrance region. As discussed in the previous section, this discrepancy arises from the saturation of the MCA, which cannot properly process signals above a certain threshold, thereby limiting its ability to register rare, high-energy secondary fragments. The contribution of secondary particles has a significant impact on the average values of the $\bar{y}_D$, while it is negligible for the $\bar{y}_F$. This is because $\bar{y}_D$, is calculated using a distribution weighted on y^2, which enhances the influence of high lineal energy events, whereas $\bar{y}_F$, is determined with a

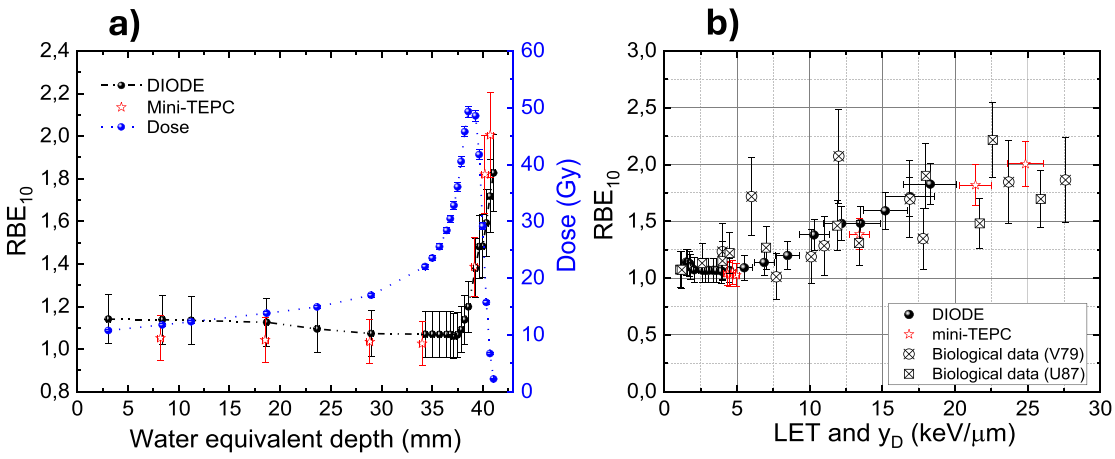

Figure 10. (a) Water depth profile of the RBE values estimated from the microdosimetric spectra weighted with Loncol's function. Solid circles represent data from the DIODE detector; open stars represent results from the mini-TEPC. The dose values calculated by the DIODE detector are also reported (right axis). (b) RBE as a function of the $\bar{y}_D$, measured with the DIODE (Filled circles) and with the mini-TEPC (empty stars) together with biological RBE10 data for V79 and U87 cells available in literature plotted as a function of the LET.

distribution weighted on y, making the contribution of such events much less significant. In addition, a noticeable deviation appears at 41.39 mm water depth, which can be attributed to the steep dose gradient in the distal fall-off and the reduced reliability of MC predictions in this region, where the signal is largely dominated by low-fluence secondary particle.

As the proton beam slow down toward the Bragg peak, their energy decreases and the nuclear reaction cross-section peaks at around 20 MeV, leading to an increased production of secondary fragments. However, when the proton energy drops below the reaction threshold (∼7 MeV), secondary particle production becomes negligible. Despite the presence of nuclear fragments, their contribution to the $\bar{y}_D$ remains limited. This is because the LET of primary protons rises steeply near the Bragg peak, making their influence on $\bar{y}_D$ dominant. Indeed, for water depth higher than 38 mm, the calculated $\bar{y}_D$, values agree with the LET_D and LET_D^{total} values as well as $\bar{y}_D^{TEPC}$.

The experimental $\bar{y}_D$ values were also compared with the simulated ones. In figure 9(b), the blue square markers represent the $\bar{y}_D^{MC}$ values simulated using MC calculations, whereas the black markers correspond to the simulated $\bar{y}_D^{MC,cut}$ values obtained by applying a cut at 65 keV μm^{-1} to the simulated microdosimetric spectra. This threshold was introduced to better represent the experimental data. The MC-simulated data with the applied cut agree very well with the experimental measurements within the experimental uncertainties, reinforcing the reliability of the microdosimetric response of the DIODE detector.

4.5. RBE calculation

Figure 10(a) shows the RBE estimation and the dose values along the proton penetration depths. The dose and RBE values are referred at the same positions, ensuring a precise correlation between physical and biological effects. The dose was calculated considering the calibration factor reported in section 3.1. The RBE is about 1.1 at entrance, increases to 1.2 in the Bragg peak and reaches values of approximately 1.8 in the distal falloff region. These values are in good agreement with those obtained with reference mini-TEPC (empty red stars in figure 10(a)), within experimental uncertainties. It is important to note that the RBE values reported here are model-based estimates referring to clonogenic survival of *in vitro* cultured cells.

By providing RBE and dose estimations in the same point and at the same time, the DIODE detector offers fast and valuable insights for optimizing radiotherapy treatment protocols, especially in ion beam therapy, where RBE varies significantly in the penetration depth in water.

Figure 10(b) shows RBE, derived from measurements performed with the DIODE detector and the mini-TEPC, as a function of $\bar{y}_D$, together with the biological RBE_{10} for V79 (Perris *et al* 1986, Prise *et al* 1990, Folkard *et al* 1996, Belli *et al* 1998) and U87 cells (Chaudhary *et al* 2014) (irradiated by monoenergetic protons) plotted against the LET. It should be noted that the $\bar{y}_D$ values closely approximate the dose averaged LET of the radiation field. The comparison in figure 10(b) is not intended as a direct validation of the microdosimetric data against radiobiological data but rather aims to demonstrate that the experimentally determined RBE values obtained with DIODE detector are consistent with proton biological RBE data reported in the literature (Guan *et al* 2015), exhibiting similar trends and comparable values. As a next step, more accurate measurements and intercomparisons with radiobiological endpoints are foreseen, aiming to

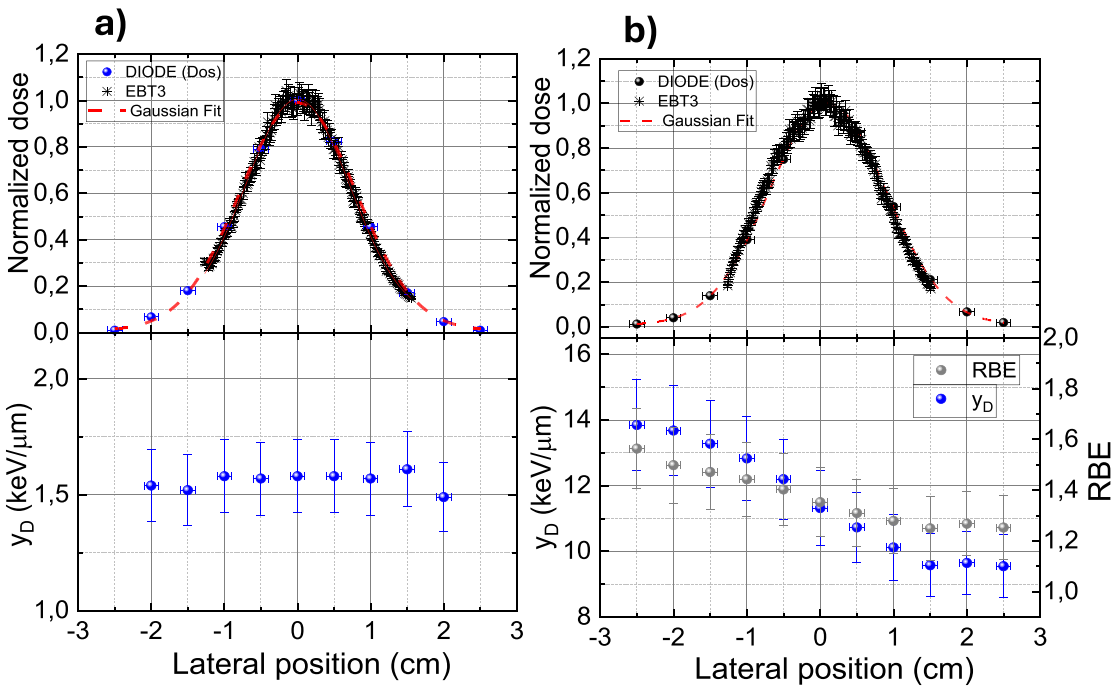

Figure 11. (a) Upper plot: normalized dose profile at entrance region measured by DIODE and EBT3; lower plot: the $\bar{y}_D$ values as a function of the lateral positions. (b) Upper plot: normalized dose profile at Bragg peak region measured by DIODE and EBT3; lower plot: the $\bar{y}_D$ and RBE values as a function of the lateral positions.

strengthen the correlation between microdosimetric and biological data. Furthermore, alternative models and methods for estimating RBE from microdosimetric spectra will be explored.

4.6. Lateral dose profiles

The lateral dose profile and energy spectra were measured by moving the DIODE detector perpendicularly to the beam direction in 5 mm steps, obtaining profiles in the *x*-direction. The detector positioning uncertainty is estimated to be ± 1 mm. The lateral dose measurements using EBT3 film was also performed. At the entrance region, the dose profiles measured by both the detectors are reported in figure 11(a) (upper plot). A good agreement is observed between the two measurements, although the limited size of the EBT3 film (3×3 cm^2 in size) prevents a full reconstruction of the whole beam profile, as evidenced by the inset in the figure. By fitting the data points with a Gaussian function, the full width at half maximum (FWHM) of the proton beam is determined to be approximately 18 mm and 17 mm, for the DIODE detector and EBT3 film, respectively. The measured values are consistent with those reported by Tommasino *et al* (2017), calculated at the isocenter. The slightly larger value measured with the DIODE detector can be attributed to its larger sensitive area as well as the fact that the beam profile was extrapolated at approximately 3 mm WE depth. As clearly seen in figure 11(a) (lower plot), the $\bar{y}_D$ values remain almost constant within the measured dose profile.

The dose profile measurement was repeated at a WE depth of 39.5 mm (near the Bragg peak region), using an RW3 slab in front of the detector. Upper plot of figure 11(b) shows the dose profile measured with the DIODE detector and EBT3 film at the Bragg peak. Overall, the dose profile measured with the DIODE detector is consistent with that obtained using the EBT3 film within the measurable range, considering that the beam width exceeds the film dimensions. A slight lateral misalignment of a few millimetres is observed in the dose profile measured by the DIODE detector.

From the Gaussian fit, the FWHM is estimated to be approximately 20 mm for both detectors, indicating a slightly broadening of the beam. Indeed, protons traversing matter undergo multiple Coulomb scatterings, leading to lateral spreading of the beam. In lower plot of figure 11(b), the $\bar{y}_D$ and RBE values at lateral positions are reported. In this case, a reduction of $\bar{y}_D$ from approximately 14 keV μm^{-1} to 9.5 keV μm^{-1} is observed, accompanied by a variation in RBE from about 1.6 to 1.2, as the detector is moved along the *x*-axis from negative to positive coordinates. The variation in $\bar{y}_D$ suggests a difference in the LET of protons along the lateral beam profile.

Figure 12 illustrates the microdosimetric spectra recorded at the two extreme lateral positions at the same water-equivalent depth of approximately 39.5 mm. A noticeable shift in lineal energy is observed between the

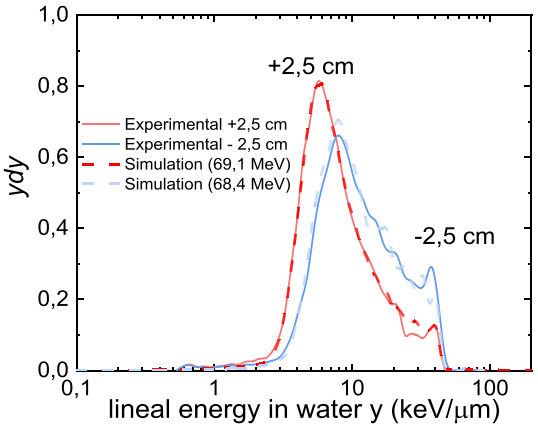

Figure 12. Comparison of experimental and simulated microdosimetric spectra measured at lateral positions ±2.5 cm.

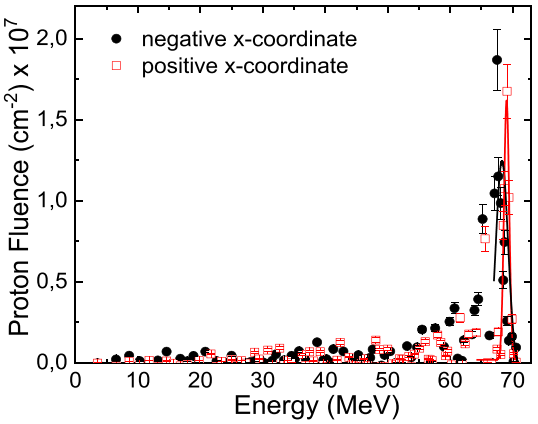

Figure 13. Reconstructed incident proton energy spectra at two lateral positions of the EBT3 film stack.

spectra corresponding to +2.5 cm and −2.5 cm positions. Figure 12 shows also a good agreement between the experimentally measured spectra at these two positions and those obtained through MC simulations. The best agreement was found considering proton energies of 69.1 MeV at +2.5 cm and 68.4 MeV at −2.5 cm. This energy variation corresponds to a penetration depth difference in water of approximately 1 mm. Since this range difference is greater than the WE thickness of a single EBT3 film, it is expected to be detectable through layer-by-layer dose variation within the 120 EBT3 stack. To investigate this, the stack was analysed at two extreme lateral positions in order to evaluate variations in proton energy deposition across the field.

A previously developed and validated analytical method (Kaufman *et al* 2015) was applied to reconstruct the incident proton energy spectrum from the dose measured in the EBT3 stack. This method takes advantage of the energy-dependent response of each film layer, which allows discrimination of protons with different energies. The algorithm progressively subtracts the dose recorded in the last irradiated layer from the preceding ones, using specific weighting coefficients calculated with SRIM (Ziegler *et al* 2010), thus enabling the reconstruction of the incident energy spectrum.

Figure 13 shows the incident proton energy spectra reconstructed using this method at two lateral positions, spaced approximately 2.4 cm apart, of the EBT3 film stack. By applying a Gaussian fit to the reconstructed spectra, a rough estimate of the most probable proton energy can be extracted, yielding 69.0 ± 0.5 MeV at the positive x-coordinate and 68.2 ± 0.8 MeV at the negative x-coordinate. The Gaussian fit is introduced as an empirical tool to provide a qualitative comparison between spectra and it does not reflect an underlying physical mode The spectra exhibit an energy difference of approximately 800 keV between the two positions, confirming the findings obtained with the DIODE detector.

It is important to note that this difference in proton energy was too small to be detected by the DIODE detector at the entrance region, where the proton LET varies slowly.

The measured lateral variation in proton energy might be likely related to beam transport effects and to the energy selection process in the delivery system. Factors such as slight differences in the path length of protons due to magnetic deflection and the inherent energy spread of the extracted beam could contribute to this phenomenon. Although the achromaticity observed was measured on the research beam line, the underlying accelerator and beam optics are shared with the clinical lines. Therefore, similar energy dispersion effects might also be present in clinical delivery systems, highlighting the relevance of extending such microdosimetric investigations to patient treatment lines. Such slight effects, evidenced only by the fine radiation quality assessment, while not appearing in a pure dosimetric profile measurement, may have a non-negligible role in the radiobiological effectiveness of irradiated targets.

These findings demonstrate that the DIODE detector is a suitable tool for such measurements. While the Dos quantifies the average absorbed dose across lateral positions, μDos characterizes in the same position the stochastic fluctuations of energy deposition within micrometer scale, providing simultaneously information on the LET and RBE of the radiation field. It is worth noting that other approaches, such as optically stimulated luminescence detectors (OSLDs) and fluorescent nuclear track detectors, have recently been proposed for passive assessment of dose, LET, and RBE in clinical proton beams (Christensen *et al* 2022, Muñoz *et al* 2024). While effective, these techniques require post-processing and are not applicable to real-time dosimetry. In contrast, the DIODE detector provides 'online' microdosimetric data. In addition, this capability makes the detector particularly useful for applications where both dose and radiation quality need to be assessed with high spatial resolution.

5. Conclusions

This study presents the experimental characterization of the DIODE detector under 70 MeV proton beams, demonstrating its capability for simultaneous dosimetric and microdosimetric measurements. The detector exhibited very good linearity, minimal LET dependence, and a good agreement with reference EBT3 film dosimeter and MC simulations in both depth-dose and lateral profile measurements.

Microdosimetric analysis confirmed the detector's ability to resolve variations in lineal energy and to support model-based RBE assessment along the proton beam path. The RBE values increased with depth, reaching values up to 1.8 in the distal region, consistent with mini-TEPC data, MC predictions, and published biological RBE trends for monoenergetic proton-irradiated cell lines. This supports the detector's potential as a physical surrogate for biological dose estimation. However, the adopted acquisition system limited the detection of rare high-LET secondary particles, particularly in the entrance region. Optimizing the dynamic range of the acquisition chain will be essential to fully capture these contributions and improve sensitivity to the complete radiation field.

Overall, the ability to provide, in a single compact device and in real time, accurate measurements of absorbed dose, and to derive LET and RBE through microdosimetric analysis, represents a significant advancement for beam quality assessment in proton therapy.

These features position the DIODE detector as a promising tool for integration into biologically optimized treatment planning, and advanced quality assurance protocols.

Data availability statement

All data that support the findings of this study are included within the article.

Acknowledgments

The research presented in this manuscript has been supported by INFN (Istituto Nazionale di Fisica Nucleare) DIODE project funded by INFN CSN-V.

ORCID iDs

C Verona 0000-0001-6401-3765
A Fazzi 0000-0001-5384-9962
L Bianchi 0009-0008-6436-9823
A Bianchi 0000-0002-3037-7007
E Scifoni 0000-0003-1851-5152
A Selva 0000-0001-9345-0251
F Tommasino 0000-0002-8684-9261
G Verona Rinati 0000-0003-1542-9910

References

Agostinelli S *et al* 2003 GEANT4—a simulation toolkit *Nucl. Instrum. Methods Phys. Res. A* **506** 250–303

Allison J *et al* 2006 Geant4 developments and applications *IEEE Trans. Nucl. Sci.* **53** 270–8

Allison J *et al* 2016 Recent developments in GEANT4 *Nucl. Instrum. Methods Phys. Res. A* **835** 186–225

Bachiller-Perea D, Zhang M, Fleta C, Quirion D, Bassignana D, Gómez F and Guardiola C 2022 Multi-arrays of 3D cylindrical microdetectors for beam characterization and microdosimetry in proton therapy *Front. Phys.* **10** 958648

Belli M *et al* 1998 RBE-LET relationships for cell inactivation and mutation induced by low energy protons in V79 cells: further results at the LNL facility *Int. J. Radiat. Biol.* **74** 501–9

Bianchi A *et al* 2023a Microdosimetry of a 62-MeV clinical proton beam with five detectors *Radiat. Prot. Dosim.* **199** 1968–72

Bianchi A, Selva A, Bortot D, Fazzi A, Mazzucconi D and Conte V 2025 First characterization of a multi-site microdosimeter *Med. Phys.* **52** e18005

Bianchi A, Selva A, Colautti P, Parisi A, Vanhavere F, Reniers B and Conte V 2021a The effect of different lower detection thresholds in microdosimetric spectra and their mean values *Radiat. Meas.* **146** 106626

Bianchi A, Selva A, Colautti P, Petringa G, Cirrone P, Reniers B, Parisi A, Vanhavere F and Conte V 2021b Repeatability and reproducibility of microdosimetry with a mini-TEPC *Front. Phys.* **9** 727816

Bianchi A, Selva A, Pasquato F, Rossignoli M, Minarello A, Fazzi A and Conte V 2024 Microdosimetric measurements for LET monitoring in proton therapy. The development of engineered mini-TEPCs for clinical applications: first results *Radiat. Meas.* **177** 107271

Bianchi A, Selva A, Reniers B, Vanhavere F and Conte V 2023b TOPAS simulations of the response of a mini-TEPC: benchmark with experimental data *Phys. Med. Biol.* **68** 034001

Bianchi A, Selva A, Rossignoli M, Pasquato F, Missiaggia M, Scifoni E, La Tessa C, Tommasino F and Conte V 2023c Microdosimetry with a mini-TEPC in the spread-out Bragg peak of 148 MeV protons *Radiat. Phys. Chem.* **202** 110567

Bortot D, Mazzucconi D, Pola A and Agosteo S 2024 Solid state microdosimetry of a 148 MeV proton spread-out Bragg peak with a pixelated silicon telescope *Radiat. Meas.* **176** 107220

Braby L A *et al* 2023 ICRU report 98, stochastic nature of radiation interactions: microdosimetry *J. ICRU* **23** 1–168

Chaudhary P *et al* 2014 Relative biological effectiveness variation along monoenergetic and modulated Bragg peaks of a 62-MeV therapeutic proton beam: a preclinical assessment *Int. J. Radiat. Oncol. Biol. Phys.* **90** 27–35

Christensen J B, Togno M, Bossin L, Pakari O V, Safai S and Yukihara E G 2022 Improved simultaneous LET and dose measurements in proton therapy using OSLDs *Sci. Rep.* **12** 8262

Cirrone G A P *et al* 2011 Hadrontherapy: a 4-based tool for proton/ion-therapy studies *Prog. Nucl. Sci. Technol.* **2** 207–12

Cirrone G A P, Petringa G, Cagni B M, Cuttone G, Fustaino G F, Guarrera M, Khanna R and Catalano R 2020 Use of radiochromic films for the absolute dose evaluation in high dose-rate proton beams *J. Instrum.* **15** C04029

Colautti P, Magrin G, Palmans H, Cortés-Giraldo M A and Conte V 2020 Characterizing radiation effectiveness in ion-beam therapy part II: microdosimetric detectors *Front. Phys.* **8** 550458

Conte V *et al* 2020 Microdosimetry of a therapeutic proton beam with a mini-TEPC and a MicroPlus-bridge detector for RBE assessment *Phys. Med. Biol.* **65** 245018

Davis J A, Ganesan K, Alves A D C, Prokopovich D A, Guatelli S, Petasecca M, Lerch M L F, Jamieson D N and Rosenfeld A 2014a Characterization of an alternative diamond based microdosimeter prototype *IEEE Trans. Nucl. Sci.* **61** 3479–84

Davis J A, Guatelli S, Petasecca M, Lerch M L F, Reinhard M I, Zaider M, Ziegler J and Rosenfeld A B 2014b Tissue equivalence study of a novel diamond-based microdosimeter for galactic cosmic rays and solar particle events *IEEE Trans. Nucl. Sci.* **61** 1544–51

Davis J A, Lazarakis P, Vohradsky J, Lerch M L F, Petasecca M, Guatelli S and Rosenfeld A B 2019 Tissue equivalence of diamond for heavy charged particles *Radiat. Meas.* **122** 1–9

De Nardo L, Cesari V, Iborra N, Chauvel P, Colautti P, Hérault J, Tornielli G and Conte V 2004 Microdosimetric assessment of nice therapeutic proton beam biological quality *Phys. Med.* **20** 71–77

Domingo Muñoz I, Möhl A, Schneider U and Sokol O 2024 Assessment of fluence- and dose-averaged linear energy transfer with passive luminescence detectors in clinical proton beams *Phys. Med. Biol.* **69** 135004

Doyen J, Falk A T, Floquet V, Hérault J and Hannoun-Lévi J-M 2016 Proton beams in cancer treatments: clinical outcomes and dosimetric comparisons with photon therapy *Cancer Treat. Rev.* **43** 104–12

Durante M *et al* 2023 Physical, biological, clinical, and methodological advances in particle therapy *Front. Phys.* **11** 1001–18

Folkard M *et al* 1996 Inactivation of V79 cells by low-energy protons, deuterons and helium-3 ions *Int. J. Radiat. Biol.* **69** 729–38

Guan F *et al* 2015 Spatial mapping of the biologic effectiveness of scanned particle beams: towards biologically optimized particle therapy *Sci. Rep.* **5** 9850

Guan F *et al* 2023 Dosimetric response of Gafchromic(™) EBT-XD film to therapeutic protons *Precis. Radiat. Oncol.* **7** 15–26

ICRU 1983 *Report* 36 (International Commission on Radiation Units and Measurements)

International Commission on Radiation Units and Measurement (ICRU) 2007 Prescribing, recording, and reporting proton-beam therapy *Report* No. 78 (International Commission on Radiation Units and Mea-surements)

Ishikawa H, Nakai K and Sakurai H 2021 A critical review of radiation therapy: from particle beam therapy (proton, carbon, and BNCT) to beyond *J. Pers. Med.* **11** 825

Jones B, McMahony S J and Prise K M 2018 The radiobiology of proton therapy: challenges and opportunities *Clin. Oncol.* **30** 285–92

Kaufman J *et al* 2015 Radiochromic film diagnostics for laser-driven ion beams *Proc. SPIE* **9515** 95151J

Kellerer A M and Chmelevsky D 1975 Concepts of microdosimetry. I. Quantities *Radiat. Environ. Biophys.* **12** 61–69

Lindborg L and Waker A 2017 *Microdosimetry* (CRC Press) (https://doi.org/10.1201/9781315373737)

Loncol T, Cosgrove V, Denis J, Gueulette J, Mazal A, Menzel H G, Pihet P and Sabattier R 1994 Radiobiological effectiveness of radiation beams with broad LET spectra: microdosimetric analysis using biological weighting functions *Radiat. Prot. Dosim.* **52** 347–52

Magrin G, Palmans H, Stock M and Georg D 2023 State-of-the-art and potential of experimental microdosimetry in ion-beam therapy *Radiother. Oncol.* **182** 109586

Magrin G, Verona C, Ciocca M, Marinelli M, Mastella E, Stock M and Verona-Rinati G 2020 Microdosimetric characterization of clinical carbon-ion beams using synthetic diamond detectors and spectral conversion methods *Med. Phys.* **47** 713–21

Mandapaka A K, Ghebremedhin A, Patyal B, Marinelli M, Prestopino G, Verona C and Verona-Rinati G 2013 Evaluation of the dosimetric properties of a synthetic single crystal diamond detector in high energy clinical proton beams *Med. Phys.* **40** 121702

Marinelli M, Prestopino G, Verona C and Verona-Rinati G 2016 Experimental determination of the PTW 60019 microDiamond dosimeter active area and volume *Med. Phys.* **43** 5205–12

Marinelli M, Prestopino G, Verona C, Verona-Rinati G, Ciocca M, Mirandola A, Mairani A, Raffaele L and Magro G 2015 Dosimetric characterization of a microDiamond detector in clinical scanned carbon ion beams *Med. Phys.* **42** 2085–93
Marsolat F, De Marzi L, Patriarca A, Nauraye C, Moignier C, Pomorski M, Moignau F, Heinrich S, Tromson D and Mazal A 2016 Dosimetric characteristics of four PTW microDiamond detectors in high-energy proton beams *Phys. Med. Biol.* **61** 6413
Meouchi C, Barna S, Puchalska M, Tran L T, Rosenfeld A, Verona C, Verona-Rinati G, Palmans H and Magrin G 2022 On the measurement uncertainty of microdosimetric quantities using diamond and silicon microdosimeters in carbon-ion beams *Med. Phys.* **49** 6699–715
Padilla-Cabal F, Kuess P, Georg D, Palmans H, Fetty L and Fuchs H 2019 Characterization of EBT3 radiochromic films for dosimetry of proton beams in the presence of magnetic fields *Med. Phys.* **46** 3278–84
Paganetti H *et al* 2002 Nuclear interactions in proton therapy: dose and relative biological effect distributions originating from primary and secondary particles *Phys. Med. Biol.* **47** 747–64
Paganetti H *et al* 2014 Relative biological effectiveness (RBE) values for proton beam therapy. Variations as a function of biological endpoint, dose, and linear energy transfer *Phys. Med. Biol.* **59** R419–72
Paganetti H *et al* 2019 Report of the AAPM TG-256 on the relative biological effectiveness of proton beams in radiation therapy *Med. Phys.* **46** e53–e78
Paganetti H *et al* 2025 A white paper on the relative biological effectiveness in proton therapy *Int. J. Radiat. Oncol. Biol. Phys.* **111** 2–14
Parisi G, Bianchi L, Couture P, Palitsin V, Fabbri A, Schettino G, Romano F and Verona C 2025 The border effect in diamond microdosimeters and its impact on hadron therapy applications *Phys. Med. Biol.* **70** 035003
Parisi G, Magrin G, Verona C, Verona-Rinati G, Barna S, Meouchi C, Romano F and Schettino G 2024 On the microdosimetric characterisation of the radiation quality of a carbon-ion beam and the effect of the target volume thickness *Phys. Med. Biol.* **69** 245003
Perles L A, Mirkovic D, Anand A, Titt U and Mohan R 2013 LET dependence of the response of EBT2 films in proton dosimetry modeled as a bimolecular chemical reaction *Phys. Med. Biol.* **58** 8477
Perris A, Pialoglou P, Katsanos A A and Sideris E G 1986 Biological effectiveness of low energy protons. I. Survival of Chinese hamster cells *Int. J. Radiat. Biol.* **50** 1093
Petringa G *et al* 2020 Monte Carlo implementation of new algorithms for the averaged-dose and -track linear energy transfer evaluation in 62 MeV clinical proton beams *Phys. Med. Biol.* **65** 235043
Prise K M, Folkard M, Davies S and Michael B D 1990 The irradiation of V79 mammalian cells by protons with energies below 2 MeV. Part II. Measurement of oxygen enhancement ratios and DNA damage *Int. J. Radiat. Biol.* **58** 261–77
PTCOG website n.d. Particle therapy facilities in clinical operation (available at: www.ptcog.site/index.php/facilities-in-operation-public)
Schmid G J, Koch J A, Lerche R A and Moran M J 2004 A neutron sensor based on single crystal CVD diamond *Nucl. Instrum. Methods Phys. Res. A* **527** 554
Solevi P, Magrin G, Moro D and Mayer R 2015 Monte Carlo study of micro-dosimetric diamond detectors *Phys. Med. Biol.* **60** 7069
Songke Y, Fan W, Tang L, Liao X and Liu Z 2022 A method for converting microdosimetric spectra in diamond to tissue in proton therapy *Med. Phys.* **49** 4743–54
Takata T, Shiraishi K, Kumagai S, Arai N, Kobayashi T, Oba H, Okamoto T and Kotoku J I 2020 Calculating and estimating second cancer risk from breast radiotherapy using Monte Carlo code with internal body scatter for each out-of-field organ *J. Appl. Clin. Med. Phys.* **21** 62–73
Tilly N *et al* 2021 Variable RBE in proton therapy: comparison of different model predictions and their influence on clinical-like scenarios *Radiat. Oncol.* **16** 59
Tommasino F *et al* 2017 Proton beam characterization in the experimental room of the Trento Proton Therapy facility *Nucl. Instrum. Methods Phys. Res. A* **869** 15–20
Tran L T *et al* 2022 Silicon 3D microdosimeters for advanced quality assurance in particle therapy *Appl. Sci.* **12** 328
Verona C, Cirrone G A P, Magrin G, Marinelli M, Palomba S, Petringa G and Verona-Rinati G 2020 Microdosimetric measurements of a monoenergetic and modulated Bragg peaks of 62 mev therapeutic proton beam with a synthetic single crystal diamond microdosimeter *Med. Phys.* **47** 5791–80113
Verona C, Fabbri A, Fazzi A, Bianchi L, Conte V, Petringa G, Raso A and Rinati G V 2024 Development of a compact and portable diamond-based detection system for dosimetry and microdosimetry in ion beam therapy *Rev. Sci. Instrum.* **95** 113302
Verona C, Magrin G, Solevi P, Bandorf M, Marinelli M, Stock M and Rinati G V 2018 Toward the use of single crystal diamond based detector for ion-beam therapy microdosimetry *Radiat. Meas.* **110** 25–31
Verona C, Magrin G, Solevi P, Grilj V, Jaksic M, Mayer R, Marinelli M and Verona-Rinati G 2015 Spectroscopic properties and radiation damage investigation of a diamond based schottky diode for ion-beam therapy microdosimetry *J. Appl. Phys.* **118** 184503
Zahradnik I A *et al* 2018 scCVD diamond membrane based microdosimeter for hadron therapy *Phys. Status Solidi a* **215** 1800383
Zahradnik I A, Barberet P, Tromson D, De Marzi L and Pomorski M T 2020 A diamond guard ring microdosimeter for ion beam therapy *Rev. Sci. Instrum.* **91** 54102
Ziegler J F, Biersack J P and Ziegler M D 2010 SRIM- The stopping and range of ions in matter *Nucl. Instrum. Methods Phys. Res. B* **268** 1818–23